

Article

The Effect of Strain Rate on the Deformation Behavior of Fe-30Mn-8Al-1.0C Austenitic Low-Density Steel

Jiahui Du ¹, Peng Chen ^{1,2,*}, Xianjun Guan ¹, Jiawei Cai ¹, Qian Peng ¹, Chuang Lin ¹ and Xiaowu Li ^{1,3,*}

¹ Department of Materials Physics and Chemistry, School of Materials Science and Engineering, Northeastern University, Shenyang 110819, China

² Key Laboratory for Anisotropy and Texture of Materials, Northeastern University, Shenyang 110819, China

³ State Key Laboratory of Rolling and Automation, Northeastern University, Shenyang 110819, China

* Correspondence: chenpeng@mail.neu.edu.cn (P.C.); xwli@mail.neu.edu.cn (X.L.)

Abstract: Automotive steels suffer different strain rates during their processing and service. In this study, the effect of strain rates on the tensile properties of fully austenitic Fe-30Mn-8Al-1.0C (wt.%) steel was investigated, and the dominant deformation mechanism was clarified. Conventional and interrupted tension tests and various microscopic characterization methods were carried out in this study. The results indicate that the yield strength increases with the increasing strain rate in the range of 10^{-4} – 10^{-1} s⁻¹, and a good strength–ductility combination was achieved in the sample deformed at 10^{-3} s⁻¹. In the process of straining at 10^{-3} s⁻¹, microbands and deformation twins were observed. Thus, the combination of microband induced plasticity (MBIP) together with twinning induced plasticity (TWIP) leads to a continuous strain hardening behavior, and consequently to superior mechanical properties. However, adiabatic heating that leads to the increase in stacking fault energy (SFE) and inhibits the TWIP effect, as well as thermal softening jointly induces an anomalous decrease in tensile strength at the high strain rate of 10^{-1} s⁻¹.

Keywords: strain rate; mechanical property; austenitic low-density steel; strain hardening; microstructure; deformation mechanism

Citation: Du, J.-H.; Chen, P.; Guan, X.-J.; Cai, J.-W.; Peng, Q.; Lin, C.; Li, X.-W. The Effect of Strain Rate on the Deformation Behavior of Fe-30Mn-8Al-1.0C Austenitic Low-Density Steel. *Metals* **2022**, *12*, 1374. <https://doi.org/10.3390/met12081374>

Academic Editor:
Ruslan R. Balokhonov

Received: 21 July 2022

Accepted: 15 August 2022

Published: 18 August 2022

Publisher's Note: MDPI stays neutral with regard to jurisdictional claims in published maps and institutional affiliations.



Copyright: © 2022 by the authors. Licensee MDPI, Basel, Switzerland. This article is an open access article distributed under the terms and conditions of the Creative Commons Attribution (CC BY) license (<https://creativecommons.org/licenses/by/4.0/>).

1. Introduction

As one kind of potential structural steel in the automotive industry, Fe-Mn-Al-C low-density steel has attracted increasing scientific and commercial attention, because of its light-weight which satisfies the requirements in increasing the fuel efficiency and reducing the gas emissions of automobiles [1–5]. Al alloying addition in the Fe-Mn-Al-C steels has an effect on density reduction, and per 1 wt.% Al reduces the density by 1.3% [4]. The Fe-Mn-Al-C steels could be either ferrite, austenite or ferrite-austenite duplex, depending mainly on the relative content of alloying elements [5]. Fully austenitic Fe-Mn-Al-C steels, with a high Al content in the range from 5 to 12 wt.%, Mn content between 12 and 30 wt.%, and C content between 0.6 and 2.0 wt.%, exhibit extraordinary strength-ductility combinations (UTS: 0.6–1.5 GPa; elongation: 30–100%), and the austenite phase is very stable during deformation [6–9].

During the production or service process, automotive steels are normally subjected to various strain rates. For instance, automobile steels suffer the strain rate from 10^{-1} to 10 s⁻¹ during the forming process and 10^2 to 10^3 s⁻¹ in the event of a collision. Yoo et al. [10] investigated the strain rate sensitivity of austenitic Fe-28Mn-9Al-0.8C steels. It was found that the yield strength increased with an increasing strain rate from 2×10^{-4} to 10^{-1} s⁻¹, exhibiting an overall positive strain rate sensitivity. In contrast, the ductility decreased with an increasing strain rate, due to the thermal activation in this strain rate range. Furthermore, the sensitivity of the strain rate for Fe-22Mn-0.6C-1.5Al twinning-induced plasticity steel has been also investigated by Yang et al. [11], who found that the ultimate

tensile strength and the uniform elongation decreased with increasing strain rate from 10^{-4} to 1 s^{-1} ; it is related to the fact that the deformation twins at a lower strain rate were much thinner and denser than those at a higher strain rate. Although there are some investigations on the relationship between the mechanical properties and strain rate of austenitic Fe-Mn-Al-C steels, the deformation mechanisms regarding microstructure evolution still remains unclear.

Accordingly, the present study aims to elucidate the effect of strain rate on the tensile deformation behavior of fully austenitic Fe-30Mn-8Al-1.0C (wt.%) steel. The tensile tests of solid solution samples were conducted at various strain rates. Detailed microstructural observations were performed on the lateral surface and fracture surface of the failed samples by scanning electron microscopy (SEM). For clarifying the evolution of dislocation substructures and their interactions, the microstructure of the deformed samples at the strain rate of 10^{-3} s^{-1} was characterized by transmission electron microscopy (TEM).

2. Materials and Methods

The ingots with the compositions of Fe-30Mn-8Al-1.0C (wt.%) were prepared by induction melting in a vacuum smelting furnace. In order to remove segregation zones originating from solidification, the ingots were homogenized at $1200 \text{ }^\circ\text{C}$ for 3 h and hot-rolled to the thickness of 5 mm by multiple passes at a final temperature exceeding $850 \text{ }^\circ\text{C}$, and then cooled to room temperature. Afterwards, the hot-rolled sheets were solution treated at $1050 \text{ }^\circ\text{C}$ for 1 h, followed by water quenching. The density was measured to be $6.8 \text{ g}\cdot\text{cm}^{-3}$ according to the Archimedes principle.

Tensile samples with a gauge dimension of $13 \text{ mm} \times 5 \text{ mm} \times 2 \text{ mm}$ were machined along the rolling direction. The tensile samples were initially polished using #2000 SiC paper and then electrochemically polished using 10% perchloric acid alcohol with a voltage of 25 V for 25 s. Tensile tests were performed on the samples up to failure using a universal testing machine AG-Xplus250kN (SHIMADZU, Kyoto, Japan) with the strain rates of 10^{-4} , 10^{-3} , 10^{-2} and 10^{-1} s^{-1} at room temperature. Except tensioning to fracture, interrupted tensile tests up to predetermined true strains ϵ_T of 1%, 10% and 25% were carried out at the strain rate of 10^{-3} s^{-1} for tracking the microstructural evolution during tensile deformation. For ensuring the accuracy of tensile properties, at least three tests were repeated for each condition.

The initial solution-treated samples were polished and etched in a solution of 100 mL methanol, 1 mL hydrochloric acid and 4 g picric acid, and then observed by an optical microscope Axio Imager A1m (ZEISS, Oberkochen, Germany). To reveal the microscopic deformation mechanism, the uniform deformation zone and fracture morphology of failed samples were observed using a scanning electron microscope JSM-6510A (JEOL, Tokyo, Japan). After interrupted deformation, the slices with 600 μm thick were spark cut from the deformed part of tensile samples and manually polished to the thickness of 50 μm . Then, the TEM slices were perforated under an electrolytic double spray thin-reducing instrument with 6% perchloric acid alcohol at 20 V and $-30 \text{ }^\circ\text{C}$. The microstructure characterization was performed by a transmission electron microscope Tecnai G20 (FEI, Hillsbro, OR, USA).

3. Results and Discussion

3.1. Initial Solution-Treated Microstructure

Figure 1 shows a representative optical micrograph of Fe-30Mn-8Al-1.0C steel. As illustrated in Figure 1a, uneven equiaxed fine grains and some annealing twins were observed in hot-rolled steel. In order to eliminate the residual stress in hot-rolled steel and obtain uniform single-phase austenite structure, the samples were solution treated at $1050 \text{ }^\circ\text{C}$ for 1 h, and the average grain size of the solid solution treated steel is calculated to be approximate 35 μm (Figure 1b). Single austenite phase with a great deal of annealing twins (up to 57%) could be observed. C and Mn are austenite stabilizing elements, and the addition of high content of Mn and C results in a stable single austenite phase. In addition,

Al has a suppressive effect on the precipitation of some carbides (such as cementite), inducing more C enrichment in austenite [12]. The annealing twins could effectively improve the properties of metallic materials by increasing the proportion of austenite grain boundary and refining the austenite grains.

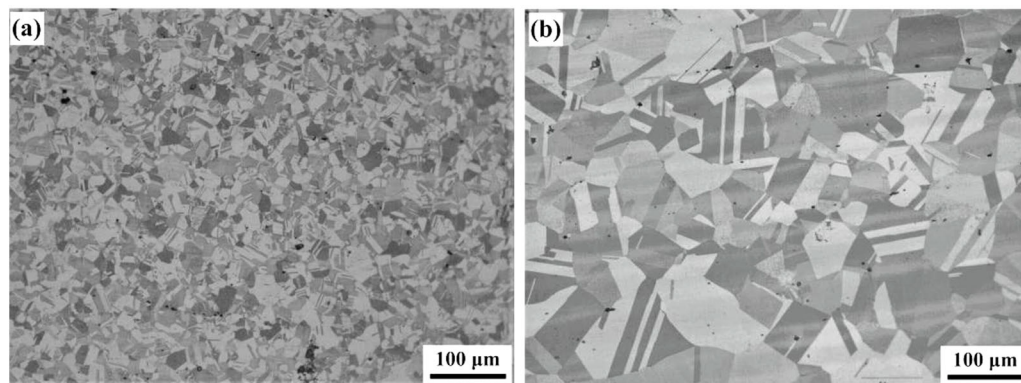


Figure 1. Optical micrograph of Fe-30Mn-8Al-1.0C steel. (a) Hot-rolled steel; (b) solid solution steel treated at 1050 °C for 1 h.

3.2. Tensile Properties

In order to examine the effect of the strain rate on the mechanical properties, uniaxial tensile tests were conducted on the solution-treated Fe-30Mn-8Al-1.0C steel at strain rates ranging between 10^{-4} and 10^{-1} s $^{-1}$. The representative stress–strain curves and the strain hardening rate curves of the steels tested at room temperature with different strain rates are presented in Figure 2. The mechanical properties are listed in Table 1. The studied steel exhibits a continuous yield behavior and a high strain hardening ability during tensile deformation under all strain-rate conditions. The yield strength increases with increasing strain rate, which are 301 ± 30 , 329 ± 20 , 378 ± 5 and 381 ± 8 MPa at the strain rates of 10^{-4} , 10^{-3} , 10^{-2} and 10^{-1} s $^{-1}$, respectively. The ultimate tensile strength exhibits an uptrend until 10^{-2} s $^{-1}$ followed by a decline at 10^{-1} s $^{-1}$, showing a maximum of 801 ± 12 MPa. The total elongation is as high as $72 \pm 3\%$ at the strain rate of 10^{-3} s $^{-1}$. Generally, the ductility becomes weak with enhancing strength for metal materials, and the product of ultimate tensile strength and total elongation ($UTS \times e_t$) is a comprehensive performance index to characterize the strength and ductility of metallic materials. The sample deformed at the strain rate of 10^{-3} s $^{-1}$ achieves the highest product of strength and ductility of 56,800 MPa%.

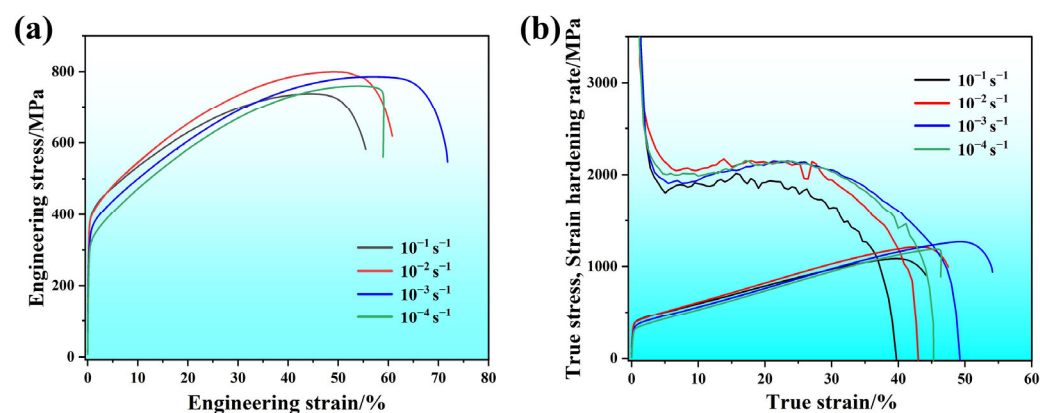


Figure 2. (a) The engineering stress–strain curves of the solution-treated Fe-30Mn-8Al-1.0C steel tested at room temperature with different strain rates, and (b) the true stress–strain curves and work hardening rate curves of the studied steel.

Table 1. Mechanical properties of the solution-treated Fe-30Mn-8Al-1.0C steel at different strain rates.

Strain Rate/s ⁻¹	Yield Strength/MPa	Ultimate Tensile Strength/MPa	Total Elongation/%
10 ⁻⁴	301 ± 30	761 ± 35	59 ± 2
10 ⁻³	329 ± 20	789 ± 25	72 ± 3
10 ⁻²	378 ± 5	801 ± 12	61 ± 1
10 ⁻¹	381 ± 8	738 ± 9	56 ± 3

Lower ultimate tensile strength and total elongation are exhibited when the sample deformed at the strain rate of 10⁻¹ s⁻¹, which is probably related to the thermal softening effect at high strain rates. Quasi-static tensile tests at the strain rate range of 10⁻⁵ to 10⁻² s⁻¹ are generally regarded as isothermal process, and it is difficult to dissipate heat to the surrounding above this strain rate range [13,14]. Thus, the adiabatic heating effect should be considered while the sample is deformed at higher strain rates. The adiabatic temperature rise ΔT can be defined by [15]:

$$\Delta T = \frac{\Delta Q}{\rho C_p} = \frac{\beta}{\rho C_p} \int_{\varepsilon_1}^{\varepsilon_2} \sigma d\varepsilon \quad (1)$$

where ΔQ is the energy converted from mechanical energy to thermal energy, which is obtained by integrating the true stress-strain curve, β is the coefficient of thermal energy converted from mechanical energy, ρ is the density of the present steel and C_p is the typical specific heat capacity. According to Equation (1), the temperature of the sample deformed at the strain rate of 10⁻¹ s⁻¹ increases by about 101 °C. For FCC materials with the high-concentration solid solution element, forest dislocations and short-range order (SRO) are the main obstacles for dislocation glide [16,17]. It is logical that the increase in the strain rate could enhance the dislocation mobility, and the dislocations would overcome obstacles more easily with the assistance of thermal energy. Additionally, the dynamic recovery of dislocations is accelerated at an increased temperature, which causes a negative effect on the strain hardening. Thereby, the strain hardening capability is weakened in the steel deformed at high strain rate. As presented in Figure 2b, the sample deformed at 10⁻¹ s⁻¹ has the lowest strain hardening rate, inducing the lowest strength and ductility. In addition, the sample deformed at 10⁻³ s⁻¹ shows the highest strain hardening ability, and consequently the best combination of strength and ductility.

3.3. Morphologies of Deformation and Fracture

The fracture surfaces of the samples deformed at different strain rates were observed by SEM, as illustrated in Figure 3. The tensile fracture characteristics of the studied steels are similar, all involving fibrous zone, radial zone and shear lip zone (Figure 3a–d). The fibrous zone accounts for the largest proportion of the fracture surface. All of the fracture surface are composed of equiaxed dimples with a bimodal size formed by a microvoid coalescence, exhibiting the characteristic of ductile fracture mode (Figure 3e–h). Thus, the samples deformed at four strain rates all exhibit good ductility (Figure 2).

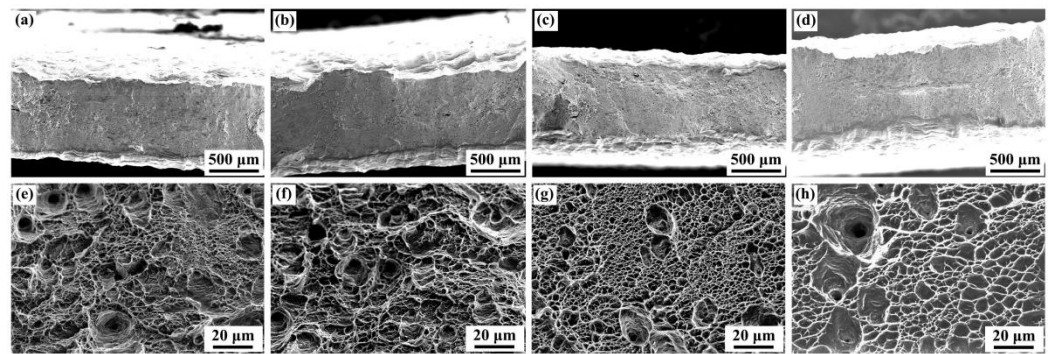


Figure 3. SEM fractographs of the samples tensioned at different strain rates of 10^{-4} s^{-1} (a,e), 10^{-3} s^{-1} (b,f), 10^{-2} s^{-1} (c,g), and 10^{-1} s^{-1} (d,h).

In addition, the distinct “snake slips” or “ripples” were observed in the inner walls of some large-sized dimples, indicating that severe plastic deformation and localized strain induce new dislocations to slip on the surface of the dimples [18]. By comparison, it is found that diameter and depth of the dimples reach a maximum in the sample deformed at 10^{-3} s^{-1} . These features indicate that the ductility of the sample deformed at 10^{-3} s^{-1} is better, which is consistent with the experimental results of mechanical properties.

Figure 4 illustrates the SEM micrographs of the lateral surface in the uniform deformation region and near fracture. At uniform deformation region, the austenite grains are elongated, and the dislocation slip characteristics are observed under all strain rates (Figure 4a–d). The dislocation slipping and the grain rotation contribute to coordinate the plastic deformation [19]. All observations reveal that there are some extrusions caused by dislocation slipping, and some microvoids are generated by the slipping extrusion at grain boundaries. Moreover, a part of slip bands pass through annealing twins to form “Z” shape slipping. For FCC materials, the stacking of {111} planes in the disrupted sequence is called a stacking fault, which is a two-dimensional defect formed by the nucleation and propagation of partial dislocations. The stacking fault has an associated energy called stacking fault energy (SFE, with units of $\text{J}\cdot\text{m}^{-2}$), since the atomic packing within it is no longer typical of the FCC structure. At the high strain rate larger than 10^{-3} s^{-1} , the adiabatic heating during deformation might increase the SFE, which has a suppressive effect on the planar slip of dislocations. On the sites near the fracture, the lateral surface becomes rougher, and the extrusion induced by dislocation slipping becomes more and more apparent (Figure 4e–f), indicating more severe plastic deformation.

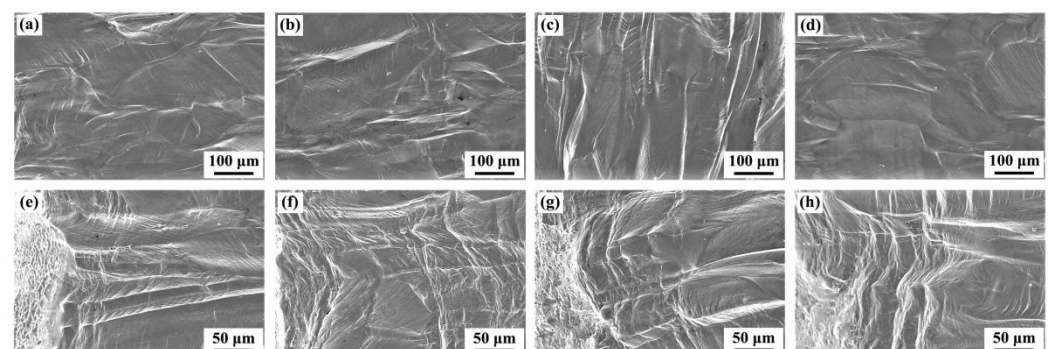


Figure 4. SEM images exhibiting the surface features at uniform deformation zones (a–d) and corresponding surface features near the fracture surfaces (e–h) of tensile samples at the strain rates of 10^{-4} s^{-1} (a,e), 10^{-3} s^{-1} (b,f), 10^{-2} s^{-1} (c,g) and 10^{-1} s^{-1} (d,h).

A few previous studies [20–22] suggested that inter/intra-granular κ -carbides and ordered L_{12} phase can be formed in solution-treated Fe-Mn-Al-C steels despite the absence of aging. Considering the promoting effect of Al on the precipitation of κ -carbides and high Al

addition, κ -carbides should exist and affect the mechanical properties of the present steel [23,24]. A coherency strain field around intragranular κ -carbides have a considerable influence on impeding the dislocation motion, resulting in the strengthening effect. By contrast, the existence of intergranular κ -carbides is conducive to the initiation and propagation of cracks, which contributes to the fracture [25]. Furthermore, L_{12} phase is regarded as short-range order (SRO), which is found to promote the planar glide of dislocations. It is usually considered that SRO could be sheared and destroyed by the leading dislocations, and then the subsequent dislocations can slip across the destroyed SRO region more easily. This effect causes the planar glide sufficiently, which is named as “glide plane softening” [17,26–29].

3.4. Microstructure Evolution during Deformation

In order to understand the microstructural evolution and related deformation mechanism during the tensile process, the interrupted tensile tests and TEM observations were conducted. Considering its good comprehensive performance of strength and ductility, the samples deformed at 10^{-3} s^{-1} , up to $\varepsilon_T = 1\%$, 10% , 25% and failure were selected for the examinations, respectively. The strain hardening rate as a function of true strain exhibits an obvious three-stage strain hardening behavior, including quick dropping, recovery and slow decreasing of strain hardening rate, as shown in Figure 5a.

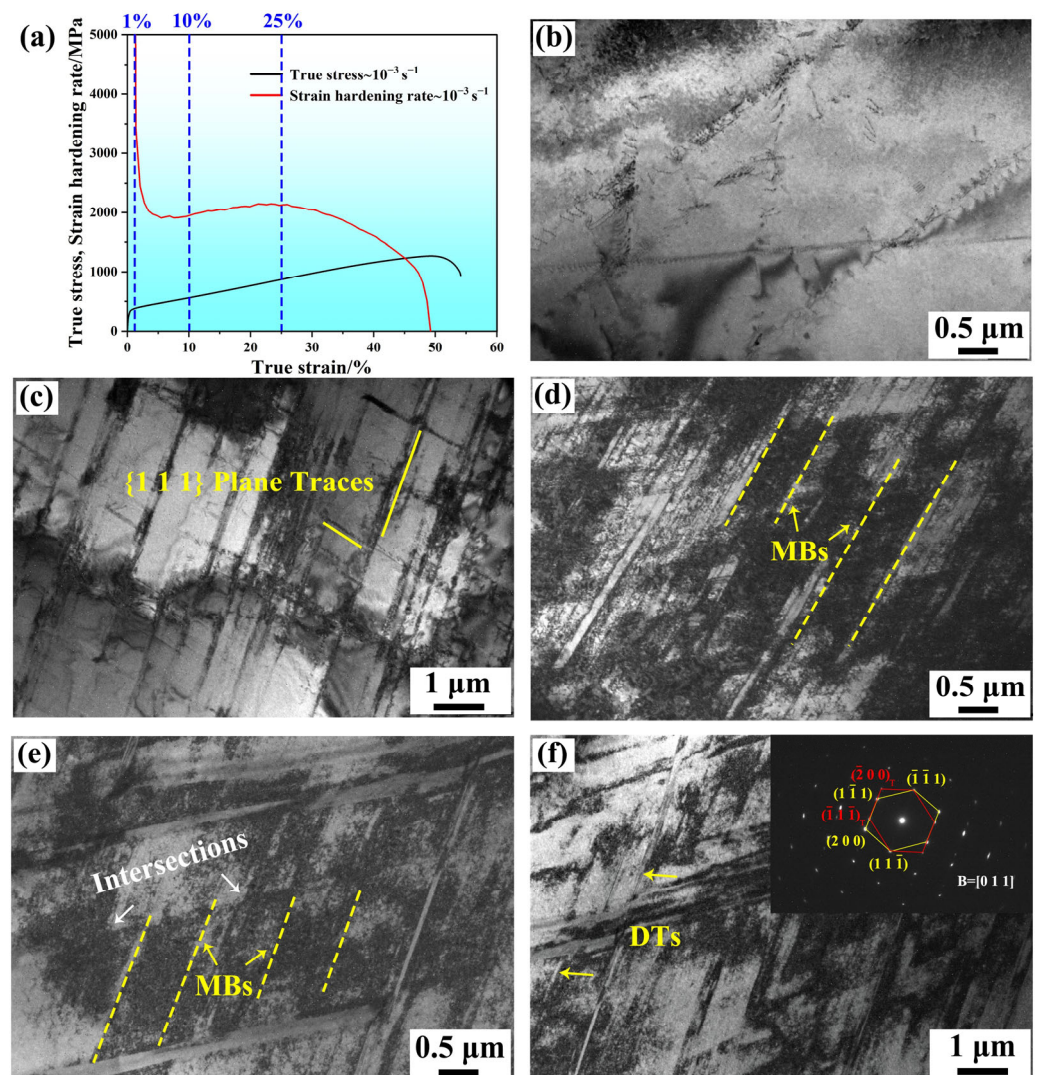


Figure 5. True stress-strain curves and strain hardening rate curves of the sample deformed at the strain rate of 10^{-3} s^{-1} (a), together with TEM micrographs of the present steel deformed to the true strains of 1% (b), 10% (c), 25% (d) and 100% (or final fracture) (e,f).

Figure 5b shows early-formed dislocation arrays aligned along the slip direction at the early deformation stage of 1% strain, which is a typical kind of planar slip dislocation configuration in FCC metals. The pronounced planar slip behavior of dislocations results in the formation of crystallographically aligned slip bands. After straining to 10%, the microstructure is still characterized by planar slip bands with a slip band spacing of approximate 700 nm (Figure 5c). The observation indicates the slip trace of two non-coplanar {111} slip planes, forming a Taylor-lattice structure, which is a kind of low energy dislocation structure [30,31]. Therefore, the planar slip of dislocations dominates the deformation mechanism at low strains.

After straining to 25%, extensive parallel high-density slip bands and microbands are found in the matrix, and the spacing of slip bands is less than 100 nm (Figure 5d). The slip bands have been evolved into high-density dislocation walls (HDDWs), which are composed of the dense dislocation bands lying on or parallel to the most active slip systems. Actually, in FCC alloys, Shockley partial dislocations slip on {111} planes and they attract or repulse each other, which are determined by the Burgers vector directions of the leading partials. If one of them is trapped by a HDDW and attracts one another, they can fuse into a sessile dislocation. During this process, further dislocation slip is hindered on both {111} planes. This causes the increase in density of HDDWs, which contributes to the barrier to the dislocation motion [32]. Moreover, Taylor lattices rotate to accommodate further strain, and a domain boundary develops from an original HDDW as a result of the misorientation between Taylor lattice domains. In the same way, a second domain boundary develops parallel to the previous one, and a microband manifested by misorientations on both sides takes shape [1,33–35].

As the strain amount further increases, well-developed microbands and their intersections are observed in fractured sample (Figure 5e). Microbands are characterized by dense tangled dislocations with a lower activity and they are usually aligned along the trace of {111} slip planes in no cell-forming FCC alloys. The microbands and their intersections can subdivide the grains. The high-density dislocations in the microbands hinder dislocation motion and decrease the effective free path of movable dislocations, resulting in the Hall-Petch strengthening effect [35,36].

The deformation twins are also observed in the microstructure of fractured sample, as confirmed by the selected area electron diffraction (SAED) patterns (Figure 5f). It indicates that the accumulated dislocations inside grains are sufficient for the activation of deformation twins. The generation of deformation twinning normally leads to an increase in plasticity of steel during deformation, namely, so-called twinning induced plasticity (TWIP) effect. Similar to the effect of microbands, the austenite grains are divided into subregions by deformation twins, which significantly refine the grain size and promote the dynamic Hall-Petch effect. Furthermore, deformation twins can impede dislocation motion, playing a very important role in promoting the dislocation accumulation and causing a reduce in the dislocation mean free path, thereby contributing to stable the strain hardening [37].

For the studied steel deformed at the strain rate of 10^{-3} s^{-1} , dislocation slip is the major deformation mode at the early stages of straining, because the flow stress is below the critical stress for twinning. With increasing strain, the continuous strain hardening is a result of microband induced plasticity (MBIP) gradually changing to microband/TWIP. The synergy of microband and twinning enhance the strengthening ability of the present steel. In addition to the thermal softening mentioned in Section 3.2, it can be inferred that the adiabatic heating at high strain rate leads to the increase in SFE and inhibits the TWIP effect, which also induces the decreases in tensile strength and work hardening rate at the high strain rate of 10^{-1} s^{-1} .

4. Conclusions

In this work, the effect of strain rate on the mechanical properties of fully austenitic Fe-30Mn-8Al-1.0C (wt.%) steel was investigated under uniaxial tension, and corresponding microstructures were examined by SEM and TEM. The following conclusions can be drawn:

(1) With the increase in strain rate, the yield strength increases from 301 MPa to 381 MPa, and the ultimate tensile strength reaches the maximum of 801 MPa at 10^{-2} s^{-1} . The recovery of work hardening rate of studied steel is the most remarkable at the strain rate of 10^{-3} s^{-1} , and its elongation reaches as high as 72%. The deterioration of its mechanical properties at 10^{-1} s^{-1} might be related to thermal softening effect and the inhibition of TWIP effect.

(2) During the tensile deformation at the strain rate of 10^{-3} s^{-1} , dislocation arrays, Taylor lattices, microbands and deformation twins can be observed in sequence with increasing strain. This indicates that the continuous strain hardening results from both MBIP and TWIP, and a good combination of strength and ductility is thus achieved.

(3) Adiabatic heating that leads to the increase in SFE and inhibits the TWIP effect, as well as thermal softening occurring at the high strain rate of 10^{-1} s^{-1} jointly induces an anomalous decrease in tensile strength at such a high strain rate.

Author Contributions: Conceptualization, X.L. and P.C.; methodology, X.L. and P.C.; validation, J.D.; formal analysis, J.D.; investigation, J.D., X.G., J.C., C.L. and Q.P.; resources, X.L. and P.C.; writing—original draft preparation, J.D. and P.C.; writing—review and editing, X.L., P.C. and J.D.; visualization, X.L., P.C. and J.D.; supervision, X.L. and P.C.; project administration, J.D. and P.C.; funding acquisition, X.L. and P.C. All authors have read and agreed to the published version of the manuscript.

Funding: This research was funded by National Natural Science Foundation of China under grant numbers 52171108 and 51804072, and also by Fundamental Research Funds for the Central University under grant number N2202007.

Data Availability Statement: The raw/processed data required to reproduce these findings cannot be shared at this time as the data also forms part of an ongoing study.

Acknowledgments: Special thanks are also due to the instrumental or data analysis from Analytical and Testing Center, Northeastern University, China.

Conflicts of Interest: The authors declare no conflict of interest.

References

1. Park, K.T. Tensile deformation of low-density Fe–Mn–Al–C austenitic steels at ambient temperature. *Scr. Mater.* **2013**, *68*, 375–379.
2. Sutou, Y.; Kamiya, N.; Umino, R.; Ohnuma, I.; Ishida, K. High-strength Fe–20Mn–Al–C-based Alloys with Low Density. *ISIJ Int.* **2010**, *50*, 893–899.
3. Choo, W.K.; Kim, J.H.; Yoon, J.C. Microstructural change in austenitic Fe–30.0wt%Mn–7.8wt%Al–1.3wt%C initiated by spinodal decomposition and its influence on mechanical properties. *Acta Mater.* **1997**, *45*, 4877–4885.
4. Frommeyer, G.; Brück, U. Microstructures and Mechanical Properties of High-Strength Fe–Mn–Al–C Light-Weight TRIPLEX Steels. *Steel Res. Int.* **2006**, *77*, 627–633.
5. Gutierrez-Urrutia, I.; Raabe, D. High strength and ductile low density austenitic FeMnAlC steels: Simplex and alloys strengthened by nanoscale ordered carbides. *Mater. Sci. Technol.* **2014**, *30*, 1099–1104.
6. Chen, S.; Rana, R.; Haldar, A.; Ray, R.K. Current state of Fe–Mn–Al–C low density steels. *Prog. Mater. Sci.* **2017**, *89*, 345–391.
7. Yao, M.J.; Dey, P.; Seol, J.-B.; Choi, P.; Herbig, M.; Marceau, R.K.W.; Hickel, T.; Neugebauer, J.; Raabe, D. Combined atom probe tomography and density functional theory investigation of the Al off-stoichiometry of κ -carbides in an austenitic Fe–Mn–Al–C low density steel. *Acta Mater.* **2016**, *106*, 229–238.
8. Ren, P.; Chen, X.P.; Cao, Z.X.; Mei, L.; Li, W.J.; Cao, W.Q.; Liu, Q. Synergistic strengthening effect induced ultrahigh yield strength in lightweight Fe30Mn11Al–1.2C steel. *Mater. Sci. Eng. A* **2019**, *752*, 160–166.
9. Moon, J.; Park, S.-J.; Jang, J.H.; Lee, T.-H.; Lee, C.-H.; Hong, H.-U.; Han, H.N.; Lee, J.; Lee, B.H.; Lee, C. Investigations of the microstructure evolution and tensile deformation behavior of austenitic Fe–Mn–Al–C lightweight steels and the effect of Mo addition. *Acta Mater.* **2018**, *147*, 226–235.
10. Yoo, J.D.; Hwang, S.W.; Park, K.-T. Factors influencing the tensile behavior of a Fe–28Mn–9Al–0.8C steel. *Mater. Sci. Eng. A* **2009**, *508*, 234–240.
11. Yang, H.K.; Zhang, Z.J.; Dong, F.Y.; Duan, Q.Q.; Zhang, Z.F. Strain rate effects on tensile deformation behaviors for Fe–22Mn–0.6C–(1.5Al) twinning-induced plasticity steel. *Mater. Sci. Eng. A* **2014**, *607*, 551–558.
12. Leslie, W.C.; Rauch, G.C. Precipitation of carbides in low-carbon Fe–Al–C alloys. *Metall. Mater. Trans. A* **1987**, *9*, 343–349.
13. Talonen, J.; Hänninen, H.; Nenonen, P.; Pape, G. Effect of strain rate on the strain-induced γ \rightarrow α' -martensite transformation and mechanical properties of austenitic stainless steels. *Metall. Mater. Trans. A* **2005**, *36*, 421–432.

14. Kundu, A.; Chakraborti, P.C. Effect of strain rate on quasistatic tensile flow behaviour of solution annealed 304 austenitic stainless steel at room temperature. *J. Mater. Sci.* **2010**, *45*, 5482–5489.
15. Curtze, S.; Kuokkala, V.-T. Dependence of tensile deformation behavior of TWIP steels on stacking fault energy, temperature and strain rate. *Acta Mater.* **2010**, *58*, 5129–5141.
16. Gerold, V.; Karnthaler, H.P. On the origin of planar slip in f.c.c. alloys. *Acta Metall.* **1989**, *37*, 2177–2183.
17. Han, D.; Zhang, Y.J.; Li, X.W. A crucial impact of short-range ordering on the cyclic deformation and damage behavior of face-centered cubic alloys: A case study on Cu-Mn alloys. *Acta Mater.* **2021**, *205*, 116559.
18. Liu, R.T. *Failure Analysis of Mechanical Parts*, 1st ed.; Harbin Institute of Technology Press: Harbin, China, 2003; pp. 103–104.
19. Wang, R.; Lu, C.; Tieu, K.A.; Gazder, A.A. Slip system activity and lattice rotation in polycrystalline copper during uniaxial tension. *J. Mater. Res. Technol.* **2022**, *18*, 508–519.
20. Kim, C.; Terner, M.; Hong, H.-U.; Lee, C.-H.; Park, S.-J.; Moon, J. Influence of inter/intra-granular κ -carbides on the deformation mechanism in lightweight Fe-20Mn-11.5Al-1.2C steel. *Mater. Charact.* **2020**, *161*, 110142.
21. Liu, J.; Wu, H.; He, J.; Yang, S.; Ding, C. Effect of κ -carbides on the mechanical properties and superparamagnetism of Fe-28Mn-11Al-1.5/1.7C-5Cr lightweight steels. *Mater. Sci. Eng. A* **2022**, *849*, 143462.
22. Cheng, W.-C.; Cheng, C.-Y.; Hsu, C.-W.; Laughlin, D.E. Phase transformation of the L1₂ phase to kappa-carbide after spinodal decomposition and ordering in an Fe-C-Mn-Al austenitic steel. *Mater. Sci. Eng. A* **2015**, *642*, 128–135.
23. Chen, P.; Fu, J.; Xu, X.; Lin, C.; Pang, J.C.; Li, X.W.; Misra, R.D.K.; Wang, G.D.; Yi, H.L. A high specific Young's modulus steel reinforced by spheroidal kappa-carbide. *Mater. Sci. Technol.* **2021**, *87*, 54–59.
24. Chen, P.; Xiong, X.C.; Wang, G.D.; Yi, H.L. The origin of the brittleness of high aluminum pearlite and the method for improving ductility. *Scr. Mater.* **2016**, *124*, 42–46.
25. Chen, P.; Li, X.; Yi, H. The κ -Carbides in Low-Density Fe-Mn-Al-C Steels: A Review on Their Structure, Precipitation and Deformation Mechanism. *Metals* **2020**, *10*, 1021.
26. Yao, M.J.; Welsch, E.; Ponge, D.; Haghighat, S.M.H.; Sandlöbes, S.; Choi, P.; Herbig, M.; Bleskov, I.; Hickel, T.; Lipinska-Chwalek, M.; et al. Strengthening and strain hardening mechanisms in a precipitation-hardened high-Mn lightweight steel. *Acta Mater.* **2017**, *140*, 258–273.
27. Kimura, Y.; Handa, K.; Hayashi, K.; Mishima, Y. Microstructure control and ductility improvement of the two-phase γ -Fe/ κ -(Fe, Mn)₃AlC alloys in the Fe-Mn-Al-C quaternary system. *Intermetallics* **2004**, *12*, 607–617.
28. Zhang, Y.J.; Han, D.; Li, X.W. A unique two-stage strength-ductility match in low solid-solution hardening Ni-Cr alloys: Decisive role of short range ordering. *Scr. Mater.* **2020**, *178*, 269–273.
29. Han, D.; Wang, Z.Y.; Yan, Y.; Shi, F.; Li, X.W. A good strength-ductility match in Cu-Mn alloys with high stacking fault energies: Determinant effect of short range ordering. *Scr. Mater.* **2017**, *133*, 59–64.
30. Gutierrez-Urrutia, I.; Raabe, D. Multistage strain hardening through dislocation substructure and twinning in a high strength and ductile weight-reduced Fe-Mn-Al-C steel. *Acta Mater.* **2012**, *60*, 5791–5802.
31. Kuhlmann-Wilsdorf, D. Theory of plastic deformation:—properties of low energy dislocation structures. *Mater. Sci. Eng. A* **1989**, *113*, 1–41.
32. Canadinc, D.; Sehitoglu, H.; Maier, H.J.; Niklasch, D.; Chumlyakov, Y.I. Orientation evolution in Hadfield steel single crystals under combined slip and twinning. *Int. J. Sol. Struct.* **2007**, *44*, 34–50.
33. Ma, B.; Li, C.; Zheng, J.; Song, Y.; Han, Y. Strain hardening behavior and deformation substructure of Fe-20/27Mn-4Al-0.3C non-magnetic steels. *Mater. Des.* **2016**, *92*, 313–321.
34. Yoo, J.D.; Hwang, S.W.; Park, K.-T. Origin of Extended Tensile Ductility of a Fe-28Mn-10Al-1C Steel. *Metall. Mater. Trans. A* **2009**, *40*, 1520–1523.
35. Yoo, J.D.; Park, K.-T. Microband-induced plasticity in a high Mn-Al-C light steel. *Mater. Sci. Eng. A* **2008**, *496*, 417–424.
36. Liu, X.; Wu, Y.; Wang, Y.; Chen, J.; Bai, R.; Gao, L.; Xu, Z.; Wang, W.Y.; Tan, C.; Hui, X. Enhanced dynamic deformability and strengthening effect via twinning and microbanding in high density NiCoFeCrMoW high-entropy alloys. *J. Mater. Sci. Technol.* **2022**, *127*, 164–176.
37. Yao, K.; Min, X. Static and dynamic Hall-Petch relations in {332}<113> TWIP Ti-15Mo alloy. *Mater. Sci. Eng. A* **2021**, *827*, 142044.